

Simultaneous 1D hybrid fs/ps rotational CARS, phosphor thermometry, and CH* imaging to study transient near-wall heat transfer processes

D. Escofet-Martin¹, A. O. Ojo¹, N.T. Mecker¹, M.A. Linne¹, B. Peterson¹

¹Institute for Multiscale Thermofluids, School of Engineering, University of Edinburgh, The King's Buildings, Mayfield Road, Edinburgh, EH9 3BF, UK.

Abstract

Near-wall transient heat transfer and flame-wall interaction (FWI) are topics of great importance in the development of downsized internal combustion (IC) engines and gas turbine technology. In this work we perform measurements using 1D hybrid fs/ps rotational CARS (HRCARS), thermographic phosphors (TGP) and CH* imaging in an optically-accessible chamber designed to study transient near-wall heat transfer processes relevant to IC engine operation. HRCARS provides single-shot gas-phase temperatures (40 μ m spatial resolution and up to 3mm wall-normal distances), while thermographic phosphors measures wall temperature and CH* measures the flame front position. These simultaneous measurements are used to resolve thermal boundary layer (TBL) development and associated gaseous heat loss for three important processes of gas/wall interactions: (1) an unburned-gas polytropic compression process, (2) FWI, and (3) post-flame and gas expansion processes. During a mild polytropic compression process, measurements emphasize that even a relatively small wall heat flux ($\leq 5\text{kW/m}^2$) yields an appreciable temperature stratification through a developing TBL. During FWI, thermal gradients induced by the flame are resolved within the TBL. Gases closest to the wall ($y < 0.2\text{mm}$) continue to experience thermal loading from polytropic compression until the flame is within $\sim 1.4\text{mm}$ from the wall. Immediately afterwards, the wall first senses the flame as the wall temperature begins to increase. During FWI, gas temperatures up to 1150K impinge on the wall, producing peak wall heat fluxes (620kW/m^2) and the wall temperature increases ($\Delta T_{\text{wall}} = 14\text{K}$). Gaseous heat loss in the post-flame gas occurs rapidly at the wall, yielding a TBL of colder gases extending from the wall as wall heat flux slowly decreases. HRCARS further captures the rapid cooling of gases in the TBL and core-gas during the mild expansion and exhaust process.

Keywords: CARS; flame-wall interaction; boundary layer; sidewall quenching.

1. Introduction

Near-wall transient heat transfer is a topic that remains insufficiently understood in combustion, but is paramount for the development of downsized internal combustion (IC) engines and low-NO_x gas turbines. Heat transfer involves the mutual interaction of hot gases and chamber surfaces. This interaction is inherent during compression (e.g., in IC engines) as the gas temperature increases exponentially, while surfaces are actively cooled. Near-wall heat transfer increases during combustion as a flame approaches the wall, inducing flame-wall interactions (FWI) [1]. The resulting heat losses to surfaces lead to parasitic energy losses, pollutant formation, and surface durability.

The accuracy with which one can predict transient heat loss is determined by the ability to resolve thermal processes within the boundary layer (BL). In engine environments, BL behavior deviates from established theory [2]; the BL is unsteady, includes chemical reactions, and the outer fluid is not constant in pressure, temperature, or velocity [3]. Most wall-functions in heat transfer models do not account for such deviations [4]. Consequently, most large eddy simulation (LES) and Reynolds-averaged Navier-Stokes (RANS) simulations employing these models cannot predict transient heat transfer accurately.

Laser diagnostics and advanced numerical simulations have been instrumental to understand transient BL behavior in combustion [3, 5–12]. Much research has primarily focused on hydrodynamic BLs (e.g., [3, 5–7]), while less research has focused on transient thermal BLs (TBL). Coherent anti-Stokes Raman spectroscopy (CARS) has been the prominent laser diagnostic technique to measure gas-phase temperature in BLs with high accuracy and precision [8–12]. The majority of CARS thermometry employ nanosecond CARS techniques, only providing 0D point-wise measurements. While such data provides useful information about the average TBL structure, the data is comprised of statistically independent (sometimes uncorrelated) events at discrete points and is insufficient to describe transient events.

Developments in short-pulse femtosecond (fs) and picosecond (ps) CARS techniques have enabled new opportunities for 1D spatially-resolved temperature and species measurements [11–14]. This is providing a renaissance of CARS for near-wall applications to study TBLs and FWI. Bohlin et al. have successfully applied hybrid fs/ps rotational CARS (HRCARS) to resolve the instantaneous TBL within a dedicated FWI burner [11, 12]. Such measurements have unmatched experimental capabilities in terms of spatial resolution (35-61 μ m) and precision (\sim 1-3%). While HRCARS has been demonstrated in near-wall applications, it has been under-utilized for heat transfer and FWI investigations. Moreover, HRCARS should be utilized with complementary diagnostics in enclosed systems to resolve the TBL processes associated with engine-related events (e.g., compression/expansion and FWI) to better understand heat transfer in engine environments.

This work utilizes HRCARS to resolve 1D wall-normal temperature profiles in a fixed-volume chamber to study heat transfer associated with transient compression/expansion and FWI processes in a sidewall quenching (SWQ) configuration. The chamber operates with a transient pressure rise/decay, simulating a mild compression/expansion process at engine timescales. HRCARS resolves the TBL with a $40\mu\text{m}$ spatial resolution for wall-normal distances up to 3mm. Thermographic phosphor (TGP) measurements and CH^* images are combined with HRCARS to provide simultaneous wall temperature measurements and track the flame front progression during compression and FWI. The combined measurements capture the transient TBL processes that describe transient heat fluxes and gas-phase thermal stratification associated with unburned gas compression, FWI, and post-flame exhaust processes.

2. Experimental setup

2.1 Chamber

Diagnostic measurements were performed in an optically-accessible, fixed-volume chamber. Figure 1 shows the relevant chamber cross-sections. The chamber features a test section (150cm^3 ; $\text{surface/volume}=2.32\text{cm}^{-1}$), a back-pressure section (6cm^3), and an orifice plate of 6mm in thickness with 81 equidistant holes (each 0.5mm diameter) that separates these sections. The test section features an inlet port, spark plug, two pressure transducers, and fused-silica windows on top and on the sides for optical access. The test section emulates a simplified IC engine geometry at top-dead-center, including a crevice region simulating a piston crevice. The crevice spacing (1.25mm) can be adjusted (0.5-5mm) by setting the position of the wall at the chamber's end.

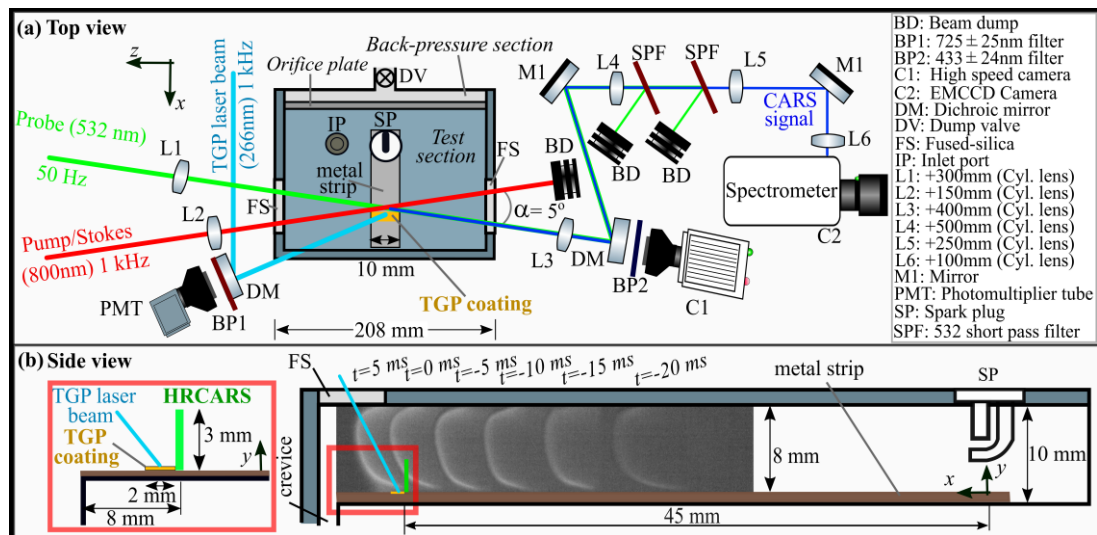


Figure 1: (a) Top view of the experimental setup for the combined 1D-HRCARS, TGP, and CH^* imaging within the fixed-volume chamber. (b) Side view of the fixed-volume chamber.

The chamber's operation is modelled after [15]. The chamber is evacuated to 20mbar using a vacuum pump. A homogeneous methane/air mixture ($\Phi=0.9$) is then introduced into the chamber ($100\text{cm}^3/\text{min}$) until reaching the desired pressure (1.02bar in this work). The mixture was ignited via the spark plug and all lasers/cameras were synchronized to ignition timing. Heat release initiates an exponential pressure rise and compresses the unburned gas ahead of the flame. At a preselected pressure (2.02bar), a dump-valve in the back-pressure section is actuated (8ms time-response). The flow is choked via the orifice plate, controlling the exiting mass flow and providing an exponential pressure decay. The firing period of the chamber is 8 minutes, and the average pressure-time curve from 42 experiments is shown in Fig. 2. The pressure rise/decay, although mild, simulates compression/expansion processes with timescales similar to IC engines. Increasing the initial pressure provides higher operating pressures, more comparable to an engine operation, and is the focus of future work.

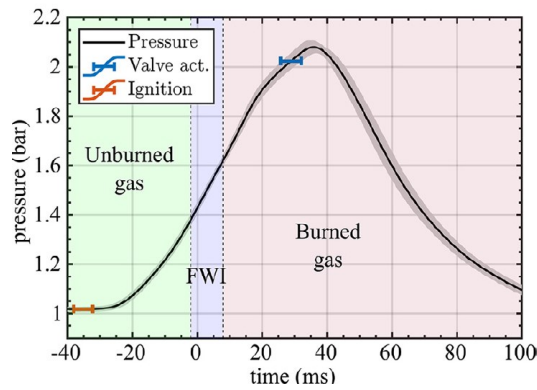


Figure 2: Chamber pressure-time curve and regimes of interest. Greyed pressures and error bars represent $\pm\sigma$.

2.2 HRCARS

The 1D-HRCARS utilizes a 2-beam phase-matching geometry [11–13]. The fs pump/Stokes pulse is generated from a Ti:Sapphire laser (Coherent, 800nm, 35fs, 7.5mJ/pulse, 9mm ($1/e^2$)) operating at 1kHz. This is locked to the 9th harmonic oscillator frequency (80MHz) of a diode-pumped Nd:YAG (Ekspla, 532nm, 22ps, 1.8cm^{-1} (FWHM), 15mJ/pulse, 5mm ($1/e^2$)) operated at 50Hz (probe pulse), producing low jitter ($<1\text{ps}$). Two translation stages are used to control the relative delays between the pump/Stokes and probe beams. A probe delay of 76ps was used. The pump/Stokes beam is pre-chirped using a pair of dispersion compensation mirrors (DCM), providing a total compensation of -440fs^2 . After propagating through 12mm of fused-silica, the pump/Stokes pulse is measured to be 37fs with a frequency-resolved optical gating (FROG) device. The pump/Stokes energy was reduced to 3mJ/pulse to suppress supercontinuum generation in the fused-silica windows. Cylindrical lenses (L1 probe; L2 pump/Stokes) were used to focus the beams into the chamber. To minimize beam steering effects a stainless steel metal strip ($50\text{mm}\times 2\text{mm}\times 10\text{mm}$, $\Delta x\times\Delta z\times\Delta y$; Fig. 1) was installed as a step on the piston surface. The center of the focused pump/Stokes and probe beams intersected above the center of this metal strip (wall) with a measurement volume (HRCARS probe volume) of $0.055\text{mm}\times 1.2\text{mm}\times 3\text{mm}$ ($\Delta x\times\Delta z\times\Delta y$). To avoid light scattered from the wall, a pair of cylindrical lenses ($f=300\text{mm}$; not shown in Fig.1) image a knife-edge into the

HRCARS probe volume. With this, the first spatial measurement position from the wall is at $y=50\mu\text{m}$. Two additional cylindrical lenses (L4, L5) image the y -axis of the HRCARS probe volume into the spectrometer entrance with a ~ 1.3 magnification ratio. Removing the knife-edge allows for direct calibration of $y=0\text{mm}$. Although beam steering during the flame propagation could bias the calibration, lenses L4 and L5 minimize this effect close to the imaging plane. A micrometer stage is used to traverse the knife-edge through the probe beam. The y -axis imaging resolution of the HRCARS probe volume is found to be $40\mu\text{m}$ (25-75% resolution).

A cylindrical lens (L3) was used to collimate the probe and anti-Stokes beams and two angle-tunable short-pass filters (SPF) were used to separate these frequencies. A cylindrical lens (L6), focussed the anti-Stokes signal into a 0.75m spectrometer (Princeton Instruments) equipped with a 1800gr/mm grating, providing a $0.28\text{cm}^{-1}/\text{pixel}$ resolution and instrument linewidth of 1.2cm^{-1} (FWHM). An EMCCD camera (Andor; $13\times 13\mu\text{m}$ pixel size) operated at 50Hz with a 1ms exposure was used to record the HRCARS signal. The CCD was binned on-chip 2×1 in the vertical direction, providing a spectral image of 149×1024 pixels. Each 1D-HRCARS spectra corresponds to $\sim 20\mu\text{m}$ in the object plane. Single-shot 1D-HRCARS spectra and example spectra at 0.3mm and 1.6mm from the wall (511K and 973K, respectively) are shown in Figs. 3a-c.

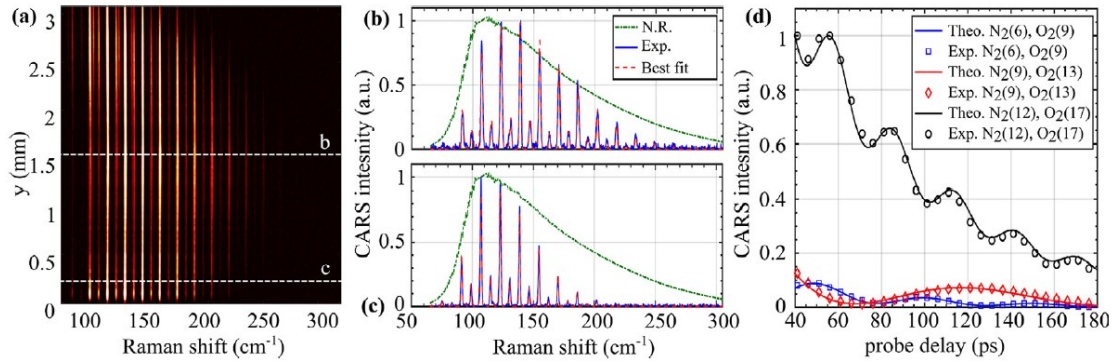


Figure 3: (a) Single-shot CCD image during the chamber exhaust at $P=1.4\text{bar}$. (b)-(c) Single-row spatially and time-resolved spectrum (Exp.) and simulated (Best fit) spectrum ((b) $T_{\text{fit}}=973\text{K}$ (c) $T_{\text{fit}}=511\text{K}$). Green line shows an averaged non-resonant argon spectrum (N.R.). (d) Beating of several $\text{N}_2\text{-O}_2$ line pairs at ambient temperature and pressure.

The 1D-HRCARS model is similar to that presented in [16, 17]. The non-resonant spectra are obtained by filling the chamber with pure argon and scanning the probe beam with respect to the pump/Stokes with 2 ps intervals. The maximum signal occurs at 0ps delay. The non-resonant spectra used in Figs. 3b-c is a weighted average from all the probe delays, and it accounts for the collection efficiencies of the optical setup. The chamber pressure, measured simultaneously with 1D-HRCARS, is used as an input parameter for the 1D-HRCARS fitting routine. Pressure dependent linewidths are included in the model [18]. The model includes self-broadened linewidths for N_2 [19] and $\text{O}_2\text{-N}_2$ for O_2 [20]. The assumption for simplified collisional partners has been discussed [11–13] for similar conditions such as the probe delay and air/fuel equivalence ratio considered in this work. Figure 3d shows three different beatings of several $\text{N}_2\text{-O}_2$ line pairs

for a 22ps probe pulse. This beating period scales inversely with the Raman shift difference between the rotational lines. Resolved rotational lines follow mono-exponential decays for N₂ when probes are longer than the fundamental rephasing period (8.38ps). For our probe delay (76ps), the measurement precision improves when removing the N₂(12) O₂(17) line pair from the fitting routine due to shot-to-shot fluctuations from the probe jitter combined with the beating. Even with the high laser fluences, at our probe delay we did not observe any evidence of a stark effect in the anti-Stokes signal [21]. The probe delay was selected to maximize the SNR at high temperatures while keeping the low temperature spectra within the dynamic range of the EMCCD. We make no quantitative claim for O₂/N₂ ratios due to the need for additional O₂ linewidth information as a function of temperature [13]. Nonetheless, there is an excellent agreement between our 1D-HRCARS model and experiments for air at ambient temperature and pressure (Fig. 3d). The ambient temperature 1D-HRCARS measurements are compared against the TGP thermometry in steady-state conditions, with deviations <1%. The precision for spatially and time-resolved 1D-HRCARS measurements at ambient temperature is $\sigma/T=0.9\%$. Temperature measurements in a McKenna burner with our 1D-HRCARS system have been benchmarked against nanosecond vibrational CARS [22] for a range of equivalence ratios of $\Phi=0.8-1.4$. Results show that temperature deviations from both CARS measuring systems are <6% (i.e. accuracy), and the HRCARS system offered very robust measurements for probe delays ranging 50-160ps. The sensitivity of rotational CARS decreases as temperature increases leading to a precision for spatially and time-resolved measurements in the McKenna burner of $\sigma/T=3\%$.

1D-HRCARS measurements are presented for $SNR \geq 15$. For instances when $SNR < 15$, the 1D-HRCARS fitting routine binned neighboring spectra to achieve $SNR \geq 15$. This was performed up to $\Delta y = 0.2\text{mm}$. If SNR remained below 15 after binning, the 1D-HRCARS spectrum was not analysed.

2.3 Thermographic Phosphors (TGP)

Wall temperatures beneath the HRCARS probe volume were measured with TGP, utilizing the luminescence lifetime methodology [23]. The TGP Gd₃Ga₅O₁₂:Cr,Ce (GGG:CrCe, Phosphor technology) was selected to measure the wall surface temperature in the chamber. The luminescence decay of GGG:CrCe exhibits temperature sensitivity between 297 - 500K [23]. A mixture of GGG:CrCe and a temperature-resistant HPC Binder, (ZYP Coatings) was deposited on the chamber's metal strip. The coating was 2mm×10mm×0.015mm ($\Delta x \times \Delta z \times \Delta y$; Fig. 1), and its edge was displaced by 0.2mm (Δx) from the HRCARS probe volume to avoid excitation by the fs/ps beams. The coating was excited by an Nd:YAG laser (InnoSlab Edgewave, 266nm, ~10ns, 0.12mJ/pulse) operating at 1kHz. The laser beam was focused, covering an area of ~2mm² on the coating, and luminescence signals were detected through the same optical access at the top of the chamber. The temperature-dependent luminescence decays were detected by a PMT equipped with a 50mm f/1.4 objective lens and a 725±25nm bandpass filter. A Tektronix MSO3054 oscilloscope was used to continuously acquire the detected luminescence signals for 2s. Luminescence decays were processed on a single-shot basis. Mean background signals within

120 μ s preceding individual luminescence decay signals were subtracted from each luminescence decay, and luminescence lifetimes were evaluated using an iterative fitting algorithm described in [24]. Temperature calibration of the luminescence lifetimes were performed by monitoring the temperature of a heated TGP-coated aluminium bar, equipped with a thermocouple and thermal insulation, which steadily cooled to ambient. For the measured temperature range (297-322K), the luminescence decay rate was 150-134 μ s, and the sensitivity was 0.73-0.54 μ s/K. Phosphor temperatures were measured with a relative standard deviation of 0.2-0.41% with accuracy of \sim 1K. In the current study, the chamber walls were not externally cooled.

2.4 CH* imaging

A high-speed camera (VEO 710L, Phantom) fitted with a 433 \pm 14nm bandpass filter was used to track the flame front (Fig. 1). The chemiluminescence captured by the camera primarily originates from CH* although broadband CO₂* contributes to a lesser extent [25]. The images were calibrated pixel-wise by imaging a target having 1mm equidistant lines placed inside the chamber. The camera operated with an exposure time of 500 μ s and at 2kHz. Images were processed to extract flame positions and their corresponding times (Fig. 1b). The reference time, $t=0$, refers to the time the flame front reaches the HRCARS probe volume at $y=2$ mm. Individual measurement times of gas temperature, wall temperature, and pressure were matched relative to this reference time.

3. Results and discussion

Figure 2 shows the averaged pressure-time trace for 42 repeated experiments. The grey area surrounding the curve represents $\pm\sigma$. Individual pressure evolution for each experiment has been time-corrected with respect to the time the flame front crosses the 1D-HRCARS probe volume at $y=2$ mm (defined as $t=0$). For a single experiment, the temporal resolution of gas temperature measurements is limited to 20ms (i.e., 50Hz probe laser repetition rate), yielding \sim 7 1D-HRCARS measurements per experiment. A time-delay between ignition and the probe pulse was varied to provide HRCARS measurements at different timings from ignition. The precise control of this time-delay and high repeatability of the chamber operation provides a coherent dataset that allows us to record and systematically study temporally evolving gas temperatures with at least 1ms intervals from ignition and increase the number of measurements during FWI ($-2\text{ms} < t < 9\text{ms}$).

This work focuses on three time-dependent regimes within the pressure-time curve (see Fig. 2). These regimes consider the relative position of the flame front with respect to the HRCARS probe volume. The unburned-gas regime occurs first with reference times $t < -2\text{ms}$ ($1.02 \leq P \leq 1.41\text{bar}$) as the flame approaches, but has not reached the HRCARS probe volume. In this regime, the unburned gases ahead of the flame are compressed due to the expansion of burned gases. The FWI regime in this SWQ configuration, is defined for reference times $-2 < t < 9\text{ms}$ ($1.41 < P < 1.6\text{bar}$) during which the flame sweeps

through the HRCARS probe volume. The final regime is the burned-gas regime ($8 < t < 100$ ms), which includes post-flame gas, peak pressure (2.1 bar), and exhaust events.

3.1. Unburned-gas regime (1.02bar-1.41bar; $t < -2$ ms)

In the unburned-gas regime, measurements are referenced by the gas pressure at which they were recorded instead of the reference time t , since pressure is the driving force for the TBL formation. Figure 4a shows unburned gas temperature profiles close to the wall ($y < 2$ mm) during the mild polytropic compression process that occurs during burned gas expansion. The 1D-HRCARS uniquely captures the TBL development and temperature gradients at the wall as a function of chamber pressure. While this mild compression process yields much lower unburned gas temperatures and pressures compared to IC engines, measurements reveal considerable thermal stratification through the BL; gas temperatures decrease 5-20K in the TBL, which is substantial in comparison to the increase in core-gas temperatures (10-30K) shown above $y=1$ mm. For initial conditions ($t < -40$ ms, 1.02bar), variations in the measured gas temperature (T_{initial}) and wall temperature (T_{wall}) are $< 1\%$. During the unburned-gas regime, the wall temperature remained constant at ~ 300 K.

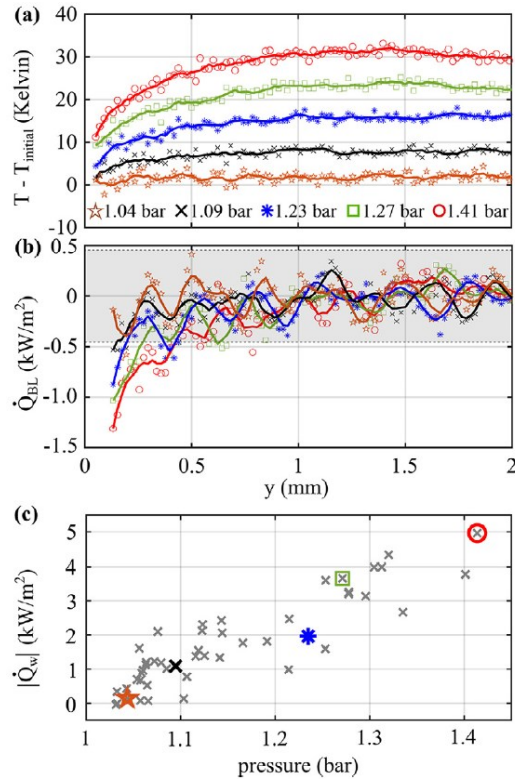


Figure 4: (a) Selected temperature profiles at different pressures (b) \dot{Q}_{BL} as a function of y , greyed region represents $\pm 3\sigma$ for $\dot{Q}_{BL}|_{1.5 < y < 2\text{mm}}$. Dots correspond to data, while lines show the $100\mu\text{m}$ moving average (trend) in (a) and (b). (c) $|\dot{Q}_w|$ versus pressure for all the temperature measurements with $t < -2$ ms.

In this analysis, we take advantage of single-shot 1D-HRCARS measurements to calculate the gaseous heat flux through the BL ($\dot{Q}_{BL} = -\lambda(300\text{K}) \cdot \partial T / \partial y \approx -\lambda(300\text{K}) \cdot \Delta T / \Delta y$). Here, λ is the gas thermal conductivity evaluated at 300K and

$\Delta T/\Delta y$ is evaluated as a moving slope with $\Delta y=180\mu\text{m}$. This analysis assumes that heat transfer is dominated by conduction, although convection may still be relevant. From the CH* images at $t=0\text{ms}$, the estimated velocity of the unburned gas is $\sim 0.67\text{m/s}$. This yields a local Reynolds number $\text{Re}_x \sim 720$, which is within the laminar regime for channel flow and suggests that conduction is dominant. For the same data shown in Fig. 4a, Fig. 4b shows that \dot{Q}_{BL} is within the $\pm 3\sigma$ of the HRCARS precision between $0.5 < y < 2\text{mm}$. However, \dot{Q}_{BL} decreases beyond the measurement precision at $y < 0.4\text{mm}$ and as temperature gradients in the TBL increase with pressure, \dot{Q}_{BL} decreases to -1.35kW/m^2 close to the wall.

For a complimentary analysis, Fig. 4c shows values of wall heat flux ($|\dot{Q}_w| = |-\lambda(T_\lambda) \cdot \partial T/\partial y| \approx |-\lambda(T_\lambda) \cdot \Delta T/\Delta y|$) calculated for all measurements acquired within the unburned gas regime. Here $T_\lambda = (T_{wall} + \overline{T}_{gas}(y=50,70,90\mu\text{m}))/2$ and $\Delta T/\Delta y = (\overline{T}_{gas}(y=50,70,90\mu\text{m}) - T_{wall})/70\mu\text{m}$. During the mild compression process, $|\dot{Q}_w|$ increases with pressure; a trend similarly observed in Fig. 4b. As $|\dot{Q}_w|$ increases up to $\sim 5\text{kW/m}^2$ at 1.41bar, temperature gradients $\Delta T/\Delta y_{\Delta y=180\mu\text{m}}$ as high as 50K/mm are present at the wall, and BL temperatures differ by up to 20K from the core-gas. To put the maximum $|\dot{Q}_w|$ of 5kW/m^2 in perspective to the thermal energy increase of the unburned gas $\Delta T \sim 30\text{K}$, this represents 3% energy loss/millisecond at the wall (assuming constant heat loss from the unburned gas to the wall). These results demonstrate that even for a mild polytropic compression process, discernible heat losses already exist at the wall, which leads to appreciable temperature stratification through a developing BL.

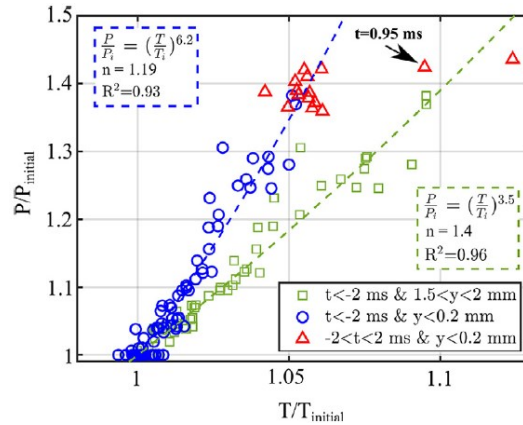


Figure 5: Polytropic compression fits for the unburned-gas regime at $t < -2\text{ ms}$ and $-2 < t < 2\text{ms}$ for $y < 0.2\text{mm}$.

The polytropic exponent is evaluated to characterize the gas-phase heat loss closest to the wall ($y < 0.2\text{mm}$) and further away from the wall ($1.5 < y < 2\text{mm}$). Figure 5 shows $P/P_{initial}$ versus $\overline{T}_{\Delta y}/T_{initial}$, where $\overline{T}_{\Delta y}$ is the spatially-averaged temperature within these regions. A best-fit polynomial trendline is used to evaluate the polytropic exponent within $P/P_{initial} = (\overline{T}_{\Delta y}/T_{initial})^{(n)/(n-1)}$. The slight scatter in data originates from the gas temperature measurements. Away from the wall, the gases experience adiabatic compression, indicated by $n=1.4$. However, for gases within $y < 0.2\text{mm}$, $n=1.19$. This emphasizes the considerable thermal stratification between the core-gas and near-wall region for discernible

heat fluxes below 5kW/m^2 . Under more realistic engine conditions with higher unburned gas temperatures and pressures, heat fluxes are anticipated to be significantly larger and lead to greater thermal stratification near walls as evidenced in [26].

3.2 FWI regime (1.4bar-1.6bar; $-2\text{ms} < t < 9\text{ms}$)

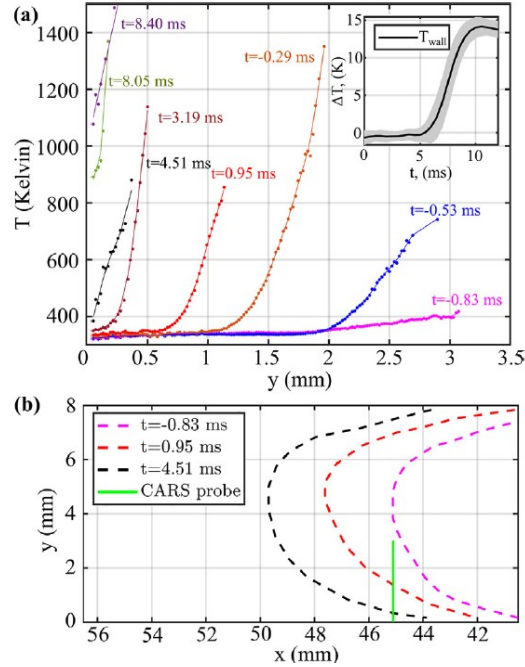


Figure 6: (a) 1D temperature profiles during FWI. Inset shows wall temperature. (b) Flame front from CH^* .

Figure 6a shows selected single-shot gas temperature profiles as the flame approaches the wall within the time interval $-2 < t < 9\text{ms}$. During FWI, not all temperature profiles span the entire 3mm measurement domain due to loss of signal. This signal loss arises at higher temperatures where $\text{SNR} < 15$, partially due to the higher temperatures, but largely due to beam steering when the flame is aligned tangentially with the HRCARS probe volume. Figure 6b shows flame profiles extracted from the CH^* images relative to the HRCARS probe volume at selected timings. The CH^* images provide valuable 2D information of the flame position and curvature with respect to the HRCARS probe volume, although CH^* images have a longer exposure ($500\mu\text{s}$) and lower spatial resolution ($\sim 166\mu\text{m}$) than 1D-HRCARS measurements.

At $t=-0.83\text{ms}$, the flame approaches the HRCARS probe volume and gas temperatures within $y=2\text{-}3\text{mm}$ begin to rise, while gases below 1.5mm continue to experience polytropic compression. Between $-0.53\text{ms} < t \leq 0.95\text{ms}$, when the flame enters the HRCARS probe volume, thermal gradients increase significantly. These flame-induced thermal gradients quickly approach the wall in comparison to thermal diffusion timescales ($\tau = l^2/D \sim 60\text{ms}$ ($l = 1\text{mm}$), $D=\text{air thermal diffusivity}$).

For reference times $t < 0.95\text{ms}$, the gases within $y < 0.2\text{mm}$ continue to experience thermal loading from polytropic compression (red triangles, Fig. 5) despite the flame rapidly approaching the wall. This suggests the presence of a layer of unburned gas that “shields” the wall from the flame. At $t=0.95\text{ms}$, the gases within $y < 0.2\text{mm}$ begin to depart from the

polytropic expression and is clearly identified in Fig. 5. All subsequent measurements with $t \geq 0.95\text{ms}$ yield higher T/T_{initial} values that fall outside of the polytropic fit. The flame induces these higher temperatures as it penetrates the protective layer of unburned gas that initially shielded the wall. At $t=0.95\text{ms}$, when unburned gases within $y < 0.2\text{mm}$ first depart from the polytropic expression, CH* images show that the flame within the HRCARS probe volume is $\sim 1.4\text{mm}$ from the wall. Meanwhile, the 1D temperature profiles at $t=0.95\text{ms}$ show significant temperature gradients starting at 0.6mm from the wall, and gas temperatures up to 850K exist 1.1mm from the wall.

Between $-0.95\text{ms} < t \leq 4.51\text{ms}$, the flame sweeps through the remaining HRCARS probe volume. At $t=3.19\text{ms}$ a very thin layer of unburned gases at the wall still exists with temperatures as low as 355K . At $t=4.51\text{ms}$, the gas closest to the wall reaches $\sim 400\text{K}$ and the wall temperature begins to increase at approximately the same time ($\sim 5\text{ms}$, see insert Fig. 6a). From $4.51\text{ms} \leq t \leq 9\text{ms}$, the qualitative shape of the flame-induced thermal profiles changes as thermal gradients near the wall are more pronounced ($> 1000\text{K/mm}$). At $t=8.4\text{ms}$, the thermal gradients lead to gas temperatures of 1150K near the wall. Within this time-frame ($4.51\text{ms} \leq t \leq 9\text{ms}$), the wall, which starts sensing the flame at $\sim 5\text{ms}$, records a peak temperature change (ΔT_{wall}) of 14K at $\sim 10\text{ms}$ (see insert Fig. 6a). This change in wall temperature is similar to values reported in fired engines [9].

3.3 Burned-gas and exhaust regime (1.6bar-2.1bar-1.1bar; $8\text{ms} < t < 100\text{ms}$)

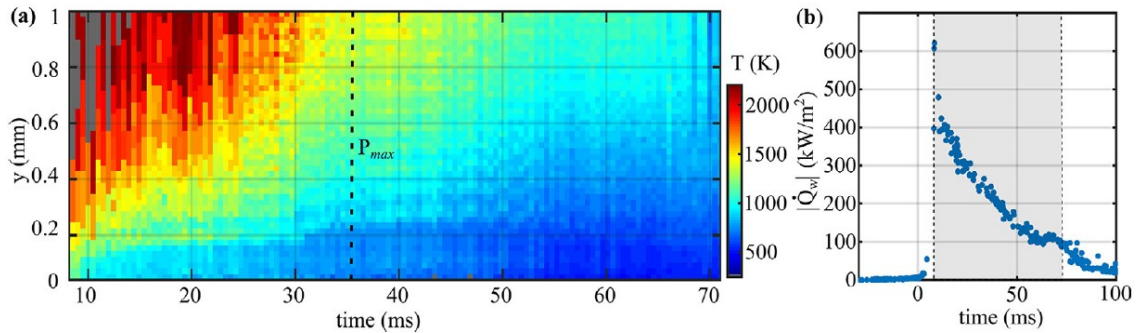


Figure 7: (a) Near-wall gas temperature for the burned-gas regime, and (b) wall heat flux with the greyed section showing the burned-gas regime within (a).

Figure 7a shows the 1D ($y < 1\text{mm}$) gas temperature evolution after the flame has swept through the HRCARS probe volume (i.e., post-flame gas). The greyed sections between $8 < t < 15\text{ms}$ and above $y=0.5\text{mm}$ in Fig. 7a, represent wall-normal spatial positions where 1D-HRCARS signals were below the SNR threshold. Between $8 < t < 35\text{ms}$, the chamber pressure continues to increase to its maximum value ($P_{\text{max}}=2.1\text{bar}$ at $t=35\text{ms}$). Despite the increasing pressure, gases nearest the wall ($y < 0.1\text{mm}$) cool down quickly from 1150K to 780K due to significant heat loss to the wall through a developing post-flame TBL. During this same time ($8 < t < 35\text{ms}$), heat is also dissipated from gases within $0.8\text{mm} < y < 1\text{mm}$ as temperatures cool from $\sim 2100\text{K}$ at $t=8\text{ms}$ to $\sim 1400\text{K}$ at $t=35\text{ms}$ when compression ends and the peak pressure is reached. Beyond $t > 35\text{ms}$, in addition to heat loss to the wall, temperatures decrease due to the decreasing pressure during expansion/exhaust.

Gas temperatures remain coldest within $y < 0.1$ mm where temperatures decrease from ~ 780 K to ~ 500 K, while gases within $0.8 \text{ mm} < y < 1$ mm decrease from ~ 1400 K to ~ 1000 K.

Figure 7b presents the heat flux to the wall $|\dot{Q}_w|$ with the maximum of 620 kW/m^2 occurring at $t = 8.40$ ms when the gas temperature within $y < 0.1$ mm peaked at 1150 K. This leads to the wall experiencing a maximum temperature increase of 14 K at $t = 10$ ms (see Fig. 6a). For $8 < t < 25$ ms, $|\dot{Q}_w|$ decreases to 280 kW/m^2 , while the core-gas ($y > 0.8$ mm) temperature remains relatively constant (2100 K) and an increase in post-flame TBL thickness is observed. Finally, during the expansion/exhaust period, $|\dot{Q}_w|$ slowly decays to $\sim 20 \text{ kW/m}^2$ around 100 ms.

4. Conclusions

Simultaneous 1D-HRCARS measurements, TGP thermometry, and CH^* imaging are conducted in an optically-accessible chamber designed to study transient near-wall heat transfer processes relevant to IC engine operation. This chamber emulates the timescales of an IC engine environment with repeatable operation, albeit having modest compression/expansion processes with peak pressures lower than IC engines. Integral measurements of gas temperature, wall temperature, and flame position are used to describe processes of gaseous heat loss and gas/flame behavior during three primary regimes of gas-wall interaction: (1) unburned-gas TBL development during a mild polytropic compression, (2) FWI in a SWQ configuration, and (3) post-flame TBL during expansion/exhaust. Despite a mild polytropic compression process, measurements show that even a relatively low wall heat flux yields appreciable temperature stratification within a developing TBL. Thermal stratification is evident within 1D temperature profiles and the polytropic exponent (n) was analysed to show that while the core-gas experiences a near-adiabatic compression ($n = 1.4$), gases within $y < 0.2$ mm deviate significantly from adiabatic ($n = 1.19$). During FWI, gases within $y < 0.2$ mm continue to experience thermal loading via polytropic compression when the flame is further than 2 mm from the wall. As the flame is ~ 1.4 mm from the wall, unburned gases within $y < 0.2$ mm are heated by the flame and deviate from the polytropic relation. Immediately afterwards, the wall first senses the flame as wall temperatures begin to increase. Recorded gas temperatures reach 1150 K at the wall, yielding a peak \dot{Q}_w of 620 kW/m^2 and a peak ΔT_{wall} of 14 K. During expansion/exhaust until $t = 72$ ms, gas temperatures decrease and continue to be ~ 500 K lower at the wall as heat is lost to the wall and a burned-gas TBL develops.

Acknowledgements

We gratefully acknowledge this work was funded by the European Research Council (ERC grant #759546) and EPSRC (EP/P020593/1, EP/P001661/1).

References

- [1] A. Dreizler and B. Böhm, Advanced laser diagnostics for an improved understanding of premixed flame-wall interactions, Proc. Combust. Inst. 35 (2015) 37–64.

- [2] H. Schlichting and K. Gersten, *Boundary-layer Theory*, 9th ed. Springer Berlin, 2017.
- [3] M. Schmitt, C. E. Frouzakis, Y. M. Wright, A. G. Tomboulides, and K. Boulouchos, Direct numerical simulation of the compression stroke under engine-relevant conditions: Evolution of the velocity and thermal boundary layers, *Int. J. Heat Mass Transf.* 91 (2015)948-960.
- [4] G. Borman and K. Nishiwaki, Internal-combustion engine heat transfer, *Progress in Energy and Combustion Science.* 13 (1) (1987) 1-46.
- [5] P. C. Ma et al., Development and Analysis of Wall Models for Internal Combustion Engine Simulations Using High-speed Micro-PIV Measurements, *Flow, Turbul. Combust.* 98 (1) (2017) 283-309.
- [6] A. Y. Alharbi and V. Sick, Investigation of boundary layers in internal combustion engines using a hybrid algorithm of high speed micro-PIV and PTV, *Exp. Fluids* 49 (4) (2010) 949–959.
- [7] C.-P. Ding, B. Peterson, M. Schmidt, A. Dreizler, and B. Böhm, Flame/flow dynamics at the piston surface of an IC engine measured by high-speed PLIF and PTV, *Proc. Combust. Inst.* 37 (4) (2019) 4973–4981.
- [8] H. Kosaka et al., Wall heat fluxes and CO formation/oxidation during laminar and turbulent side-wall quenching of methane and DME flames, *Int. J. Heat Fluid Flow* 70 (2018) 181–192.
- [9] R. P. Lucht, D. Dunn-Rankin, T. Walter, T. Dreier, and S. C. Bopp, Heat Transfer in Engines: Comparison of CARS Thermal Boundary Layer Measurements and Heat Flux Measurements, SAE Technical Paper 910722 (1991).
- [10] B. Grandin, I. Denbratt, J. Bood, C. Brackmann, and P. E. Bengtsson, The effect of knock on the heat transfer in an SI engine: Thermal boundary layer investigation using CARS temperature measurements and heat flux measurements, SAE Technical Paper 103 (3) (2000) 2003-2016.
- [11] A. Bohlin, M. Mann, B. D. Patterson, A. Dreizler, and C. J. Kliewer, Development of two-beam femtosecond/picosecond one-dimensional rotational coherent anti-Stokes Raman spectroscopy: Time-resolved probing of flame wall interactions, *Proc. Combust. Inst.* 35 (2015) 3723-3730.
- [12] A. Bohlin, C. Jainski, B. D. Patterson, A. Dreizler, and C. J. Kliewer, Multiparameter spatio-thermochemical probing of flame-wall interactions advanced with coherent Raman imaging, *Proc. Combust. Inst.* 36 (3) (2017) 4557–4564.
- [13] J. E. Retter, G. S. Elliott, and S. P. Kearney, Dielectric-barrier-discharge plasma-assisted hydrogen diffusion flame. Part 1: Temperature, oxygen, and fuel measurements by one-dimensional fs/ps rotational CARS imaging, *Combust. Flame*, 191 (2018) 527–540.
- [14] W. D. Kulatilaka, H. U. Stauffer, J. R. Gord, and S. Roy, One-dimensional single-shot thermometry in flames using femtosecond-CARS line imaging, *Opt. Lett.* 36 (21) (2011) 4182–4184.
- [15] M. A. Linne, R. K. Mackay, and W. L. Bahn, A blow-down combustion bomb for engine in-cylinder kinetics research, *Rev. Sci. Instrum.* 65 (5) (1994) 3834-3838.
- [16] C. Yang, D. Escofet-Martin, D. Dunn-Rankin, Y. C. Chien, X. Yu, and S. Mukamel, Hybrid femtosecond/picosecond pure-rotational coherent anti-Stokes Raman scattering with chirped probe pulses, *J. Raman Spectrosc.* 48 (12) (2017) 1881-1886.
- [17] C. Yang, P. He, D. Escofet-Martin, J. B. Peng, R.W. Fan, X. Yu, D. Dunn-Rankin, Impact of input field characteristics on vibrational femtosecond coherent anti-Stokes Raman scattering thermometry, *Appl. Opt.* 57 (2) (2018) 197-207.
- [18] T. L. Courtney, N. T. Mecker, B. D. Patterson, M. Linne, and C. J. Kliewer, Hybrid femtosecond/picosecond pure rotational anti-Stokes Raman spectroscopy of nitrogen at high pressures (1-70 atm) and temperatures (300-1000 K), *Appl. Phys. Lett.* 114 (10) (2019) 101-107.
- [19] C. J. Kliewer, A. Bohlin, E. Nordström, B. D. Patterson, P. E. Bengtsson, and T. B. Settersten, Time-domain measurements of S-branch N₂-N₂ Raman linewidths using picosecond pure rotational coherent anti-Stokes Raman spectroscopy, *Appl. Phys. B Lasers Opt.* 108 (2) (2012) 419-426.
- [20] G. Millot, R. Saint-Loup, J. Santos, R. Chauv, H. Berger, and J. Bonamy, Collisional effects in the stimulated Raman Q branch of O₂ and O₂-N₂, *J. Chem. Phys.* 96(2) (1992) 961-971.
- [21] A. Hosseinnia, M. Ruchkina, P. Ding, P.-E. Bengtsson, and J. Bood, Simultaneous temporally and spectrally resolved Raman coherences with single-shot fs/ns rotational CARS, *Opt. Lett.* 45 (2) (2020) 308-311.

- [22] P. Weigand, R. Lückcrath, and W. Meier, Documentation of flat premixed laminar CH₄/air standard flames: temperatures and species concentrations, available at <https://www.dlr.de/vt/desktopdefault.aspx/tabid-3065/4632_read-6696/>.
- [23] N. Fuhrmann, C. Litterscheid, C. P. Ding, J. Brübach, B. Albert, and A. Dreizler, Cylinder head temperature determination using high-speed phosphor thermometry in a fired internal combustion engine, *Appl. Phys. B Lasers Opt.* 123 (2014) 110.
- [24] J. Brübach, J. Janicka, and A. Dreizler, An algorithm for the characterisation of multi-exponential decay curves, *Opt. Lasers Eng.* 47 (1) (2009) 75-79.
- [25] Y. Hardalupas and M. Orain, Local measurements of the time-dependent heat release rate and equivalence ratio using chemiluminescent emission from a flame, *Combust. Flame*, 139 (3) (2004) 188-207.
- [26] B. Peterson, E. Baum, B. Böhm, V. Sick, and A. Dreizler, Evaluation of toluene LIF thermometry detection strategies applied in an internal combustion engine, *Appl. Phys. B* 117 (2014) 151-175.